CrossMark

# The Application of Permanent Magnet Synchronous Motor with Small Electrical Time Constant in Fiber Positioner

Shaoxiong Guo[1], Yan Yang[2], Yanbin Yin[1], Yihu Tang[1], Yang Tian[1], and Chao Zhai[3]

[1] Department of Precision Machinery and Precision Instrumentation, University of Science and Technology of China, Hefei 230026, China
[2] School of Biomedical Engineering, Division of Life Sciences and Medicine, University of Science and Technology of China, Hefei 230026, China
[3] Experiment Center of Engineering and Material Science, University of Science and Technology of China, Hefei 230026, China; zhaichao@ustc.edu.cn

## Abstract

With the development of cutting-edge multi-object spectrographs, fiber positioners located in the focal plane are being scaled down in size, and miniature hollow-cup Permanent Magnet motors are now being considered as a suitable replacement for Faulhaber Precistep stepper motors. However, the small electrical time constant of such coreless motors poses a challenge, as the problem of severe commutation torque ripple in a fiber positioner running a position loop has been tricky. To overcome this challenge, it is advised to increase the Pulse Width Modulation (PWM) frequency as much as possible to mitigate the effects of the current fluctuation. This must be done while ensuring adequate resolution of the PWM generator. By employing a voltage open-loop field-oriented control based on a modulation frequency of 1 MHz, the drive current only costs 25 mA under a 3.3 V power supply. The sine degree of phase current is immaculate, and the repeat positioning accuracy can reach 2 $\mu$m. Moreover, it is possible to further shrink the bill of devices and the layout area of the Printed Circuit Board, especially in size-sensitive applications. This device has been developed under the new generation of The Large Sky Area Multi-Object Fiber Spectroscopic Telescope.

*Key words:* instrumentation: adaptive optics – instrumentation: spectrographs – proper motions – reference systems

## 1. Introduction

The powerful Multi-Object Spectroscopy survey is a fascinating area of study for astronomers worldwide. It offers the unique capability of simultaneously observing and studying the formation and evolution of galaxies (Xiangqun et al. 2012), the search for dark matter and dark energy (Flaugher 2006), and the characterization of exoplanets. This impressive feat is the result of decades of tireless efforts by researchers who have focused on large-scale spectral measurements. The establishment of many MOS (Multi-Object Spectroscopy) telescope projects has been crucial to this field. Among these projects are MOONS (The Multi-Object Optical and Near-infrared Spectrograph) (Cirasuolo et al. 2014), LAMOST (The Large Sky Area Multi-Object Fiber Spectroscopic Telescope) (Cui et al. 2004), and DESI (The Dark Energy Spectroscopic Instrument) (Diehl et al. 2010). These projects have significantly improved the parallel observation capability of MOS and achieved large-scale spectral observations. To further enhance the parallel observation capability of MOS, a large number of SCARA (Selective Compliance Assembly Robot Arm) robotic arms have been arranged on the focal plane of the above telescope system. These robotic arms are used to quickly and accurately place the spectral receiving fibers to collect faint spectra from stars and galaxies (Kronig et al. 2020). The parallel working SCARA robotic arms have become the most critical component

in the fiber positioning system, and they are called fiber positioners. Figure 1 explains the schematic of the double rotary structure of the classic fiber positioner, also known as the RR planar kinematics (Kronig et al. 2018).

In the pursuit of more efficient and parallel observation of celestial targets, modern multi-spectral sky surveys require a greater quantity and smaller size of fiber positioners. To this end, the volume of motors used to drive rotating shafts is developing toward miniaturization, according to research (Hu et al. 2014; Sayres et al. 2021). Despite this trend, Faulhaber Precistep stepper motors remain one of the preferred solutions for many fiber positioner designs, such as those in MEGARA (Pérez-Calpena et al. 2018), LAMOST (Hu et al. 2004), and MOONS (Montgomery et al. 2016). However, the smallest stepper motor currently available is only $\phi$6 mm (ref Faulhaber), and stepper motors also possess a passive holding torque. This means that when the power is turned off, the stepper motor must stop at a certain full step, requiring a high reduction ratio. Nowadays, with the low efficiency of the stepper motor working mode and its larger physical size, smaller-sized miniature brushless DC motors have emerged as a more suitable option for future downscaling of the design. Brushless DC motors, unlike stepper motors, do not have the full-step stop problem. However, it should be noted that some brushless DC motors do possess cogging torque. Araujo et al. (2020)
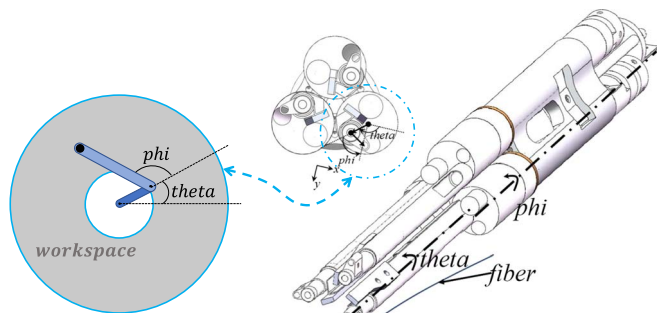
**Figure 1.** Two rotating axes rotate by angles theta and phi, respectively, and the optical fiber (black) at the end of the axis can be freely positioned to cover the gray annular workspace (adapted from Guo et al. 2022).

have observed this phenomenon and noted that when powering off the motor coils, the axis might slightly move during their tests. The solution to this issue is to apply a small current into the motor coil to keep the position, causing additional thermal dissipation. In order to address the issue of cogging torque, Hörler et al. (2018) chose a hollow-cup Permanent Magnet (PM) motor without cogging torque for the DESI project. Their motor drive module can be directly turned off to enter low-power mode during the focal plane exposure, which is essential to develop astronomical instruments. This is because unnecessary power consumption can impact the signal-to-noise ratio if important temperature gradient are created, producing turbulent air flows near the focal plate (Fahim et al. 2015).

The DESI has successfully deployed and implemented fiber positioners driven by $\phi 4$ mm hollow-cup brushless DC motors (Martini et al. 2018). This innovation has allowed for greater efficiency and smaller size compared to the original stepper motors that were used. The new generation of LAMOST is also considering utilizing more efficient and smaller-sized brushless DC motors to replace the original stepper motors. However, the adoption of miniature hollow-cup motors also presents new challenges in terms of positioning control technology. Accurately placing the fibers at the target point is crucial for improving the spectral reception capacity of the telescope system. Therefore, the development of advanced positioning control technology for miniature hollow-cup motors is an urgent issue that needs to be addressed.

The hollow-cup PM motor is a novel type of permanent magnet brushless DC motor (BLDCM) that has recently become popular in the field of fiber positioner. The distinctive feature of this motor is that it lacks iron laminations in its armature, which completely eliminates the stator slots and magnetic saturation issues that are common in traditional iron-core motors (Park et al. 2000; Liu et al. 2008). This reduction in stator slots and magnetic saturation leads to a significant decrease in cogging torque ripple and reluctance (Zhou & Fang 2013; SUN et al. 2022), which makes it possible for the

fiber positioner to cut off the power to the motor coils during focal plane exposure without any slight movement of the fiber. This measure is critical because it ensures good seeing of the telescope system (Sosa et al. 2017) and prevents the creation of seeing-degrading thermal plumes in the telescope field of view (Besuner et al. 2012). Therefore, the hollow-cup PM motor is expected to become more widely adopted in fiber positioner in the near future.

As we embark on the path of understanding miniature-sized hollow-cup PM motors, we encounter a perplexing dilemma. The coreless windings with a low inductance pose a formidable obstacle in drive control, leading to severe torque ripple that can be difficult to tame. It is worth noting that the larger-sized hollow-cup PM motors seem to be better equipped to handle such a situation, as research indicates (Zhou & Fang 2013; Aydin & Gulec 2016). However, the miniature-sized hollow-cup PM motors are constrained by their compact size, and their windings are fashioned from fine copper wire, which imbues them with higher impedance. This high impedance, in turn, causes the electrical time constant to shrink significantly, giving rise to a host of challenges in attaining a smooth spin of the motor. Therefore, in this article, we aim to explore this issue further and uncover potential solutions by working with a $\phi 4$ mm hollow-cup PM (supplied by NAMIKI Precision Jewel Co., Japan).

We organize the paper as follows. In Section 2, we demonstrate the typical characteristics of miniature hollow-cup PM used in a fiber positioner, namely a very small electrical time constant, and analyzes the impact of such characteristic on commutation current ripple from the perspective of drive control. The expression of current ripple in time domain is deduced in Section 3. In Section 4, we verify the idea with relevant hardware and figure out that upper limitation of the resolution of Pulse Width Modulation (PWM) generator would also play an important role in practical applications, i.e., power bridge's signal-level delay and timer's upper frequency. A high carrier frequency control method based on open-loop field-oriented control (FOC) is deployed in fiber positioner for validation in Section 5 and performance and test results of fiber positioner are discussed in Section 6. We conclude in Section 7.

## 2. Characteristics of Miniature-sized Hollow-cup PM

Generally, BLDCM has three kinds of torque ripple (Zeroug et al. 2002):

1. The reluctance torque caused by the interaction of the stator magnetomotive forces with the angular variation of the rotor magnetic reluctance.
2. The cogging torque resulting from the interaction of the magnet and the stator tooth.
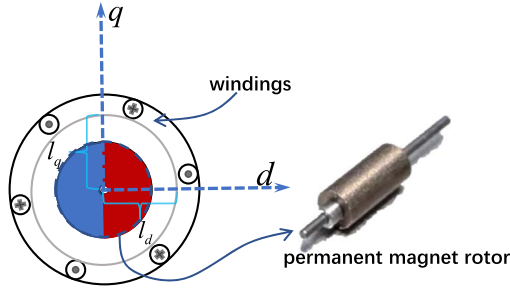
**Figure 2.** Left : Structure of miniature-sized hollow-cup PM; Right : Rotor of motor.

3. The current ripple due to PWM-controlled technology, as a consequence of periodic communication and limitation of the resolution of PWM generator (Lai et al. 2007).

From Figure 2, it is clear that miniature-sized hollow-cup PM's inner rotor is composed of a whole permanent magnet due to physical limitation, i.e., there is no cogging structure and corresponding torque ripple. The reluctance torque, as presented in Equation (1) (Guo et al. 2022):

$$\tau' = \frac{3(L_d - L_q)}{4 L_d L_q} \, |\varphi_s|^2 \sin 2\delta. \tag{1}$$

Taking the rotor coordinates $(d-q$ axes) of the motor as reference coordinates (Casadei et al. 2002), $L_d$, $L_q$ are respectively $d-$ and $q-$ axis inductance, $\delta$ represents angle between stator flux and rotor, and $\varphi_s$ is the flux generated by stator.

Reluctance torque $\tau'$ is apparently correlated to $L_d$, $L_q$. Equation (2) describes definition of inductance.

$$L = \frac{T_{\mathrm{ph}}\phi}{I} = \frac{T_{\mathrm{ph}}F}{I\mathfrak{R}} = \frac{T_{\mathrm{ph}}T_{\mathrm{ph}}I}{I\mathfrak{R}} = \frac{T_{\mathrm{ph}}^2}{\mathfrak{R}}. \tag{2}$$

where $L$ is single phase inductance, $T_{\mathrm{ph}}$ stator winding turns, $I$ phase current, $\phi$ magnetic flux, $F$ magnetomotive force (MMF), $\mathfrak{R}$ magnetic resistance of the magnetic circuit. Based on this, the inductance is inversely proportional to the resistance of the magnetic circuit. And $\mathfrak{R} = \frac{l}{\mu_0 \mu_r A}$, $\mu_0$ is permeability of vacuum, $\mu_r$ permeability of permanent magnet, $A$ cross-sectional area of magnetic circuit. We obtain inductance ratio of $d-$ axis to $q-$ as follows:

$$\frac{L_d}{L_q} = \frac{\mathfrak{R}_q}{\mathfrak{R}_d} = \frac{l_q}{l_d}. \tag{3}$$

According to Figure 2, we can conclude that $l_d$ equals $l_q$ without consideration of inhomogeneity of motor manufacture. Here, $l_d$ and $l_q$ represent the magnetic circuit length of $d-$ and $q-$ axis respectively. Basically, there is no concern of reluctance torque ripple because of $L_d = L_q$.

As it turns out, the current ripple of communication becomes a critical factor when driving a miniature-sized hollow-cup PM (Park et al. 2000). This is especially true for positioning control at low speeds, where torque vibration can be particularly significant (Fang et al. 2014). Given that the stator windings of the hollow-cup motor have no iron core, the inductance is small, the freewheeling time is brief, and the current fluctuation is violent (Fang et al. 2014), which ultimately leads to acute torque ripple (Zeroug et al. 2002). To mitigate this issue, there are generally three main techniques: Pulse-Amplitude Modulation (PAM) (Xiaofeng & Zhengyu 2006; Lai et al. 2007), upscaling the frequency of PWM (Fang et al. 2013; Tsotoulidis & Safacas 2015), and seriesing additional inductor. However, since PAM is typically used for $120°$ commutation control (Zhou et al. 2017) and is mainly adopted in high-speed operating applications, it is not suitable for sine wave control at low-speed conditions. Therefore, we will not delve deeper into it. On the other hand, upscaling the PWM frequency and adding inductance share a common principle, which we will explore in detail.

## 3. Electrical Time Constant and PWM Frequency

The concept of electrical time constant plays an essential role in understanding the performance of a $\phi 4\,\mathrm{mm}$ motor. The electrical time constant of the motor is calculated as $\tau = \frac{L_s}{r} = 2.49158\,\mu\mathrm{s}$. This time constant is an indication of how fast the motor's phase current can change in response to a change in voltage. In comparison, the mechanical time constant supplied by the motor datasheet is $9.15\,\mathrm{ms}$, which is much larger than the electrical time constant. This implies that the adjustment of the motor's phase current is much faster than the change of Back ElectroMotive Force (BEMF) generated by the rotor's rotation. In other words, the former is only less than $1/3700$ of the latter, namely, when phase current adjustment ends, BEMF almost maintains the same. Consequently, BEMF can be seen as constant during a switching period (Oliveira et al. 2007).

So the above circuit (Figure 3) can be simplified as a classical *LR* series model. We choose the seven-segment Space Vector Pulse Width Modulation (SVPWM) method to generate a smoother sine wave in the windings (Guo et al. 2022).

The count and effective level distribution of the timer during switching period are shown in Figure 4:

The phase current follows the first-order full-correspondence expression: $i(t) = i(\infty) + [i(0_+) - i(\infty)]e^{-\frac{t}{\tau}}$. BEMF constant of motor $e$ equals $0.059\,\mathrm{mV\,rpm^{-1}}$, and motor rotates uniformly at a low speed in fiber positioner, so we ignore the fluctuation of BMEF here. Besides, SVPWM modulation results in that the maximum effective value of the phase voltage equals $V_{\mathrm{bus}}^*/\sqrt{3}$, in that, $i(\infty) = V_{\mathrm{bus}}^*/\sqrt{3}\,r$, where $V_{\mathrm{bus}}^* = V_{\mathrm{bus}} - Ea$, $Ea$ remains constant. Then the current during a switching period $T$ can be derived further into:
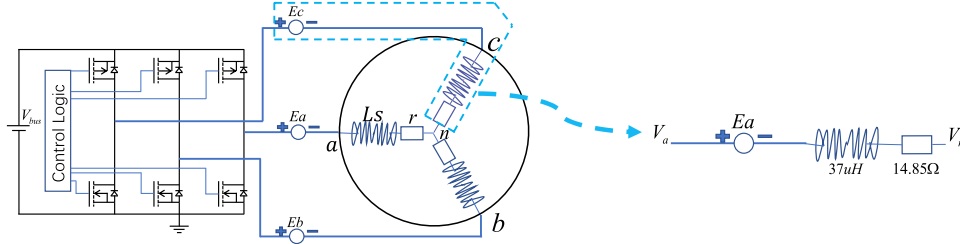
**Figure 3.** Hardware topology of motor control and single phase circuit model.
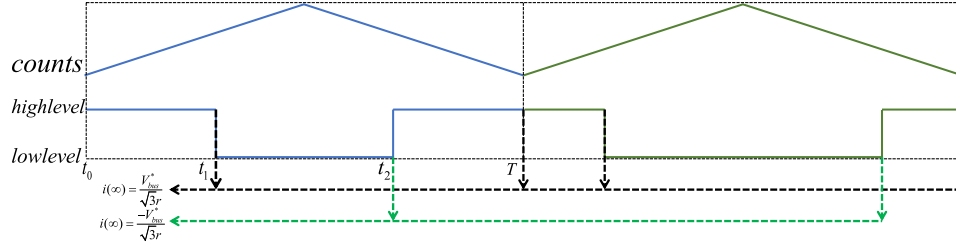


**Figure 4.** Counter and level of timer during switching cycle.

$$
i(t)
$$

$$
=\begin{cases}
\dfrac{V_{\text{bus}}^*}{\sqrt{3}\,r} + [i(0_+) - \dfrac{V_{\text{bus}}^*}{\sqrt{3}\,r}]e^{-\frac{t}{\tau}}, & 0 \leqslant t < t_1 \\[2ex]
\dfrac{-V_{\text{bus}}^*}{\sqrt{3}\,r} + \left(\dfrac{2V_{\text{bus}}^*}{\sqrt{3}\,r} + [i(0_+) - \dfrac{V_{\text{bus}}^*}{\sqrt{3}\,r}]e^{-\frac{t_1}{\tau}}\right)e^{-\frac{(t-t_1)}{\tau}}, & t_1 \leqslant t < t_2 \\[2ex]
\dfrac{V_{\text{bus}}^*}{\sqrt{3}\,r} + \left(\dfrac{-2V_{\text{bus}}^*}{\sqrt{3}\,r} + \left(\dfrac{2V_{\text{bus}}^*}{\sqrt{3}\,r} + [i(0_+) - \dfrac{V_{\text{bus}}^*}{\sqrt{3}\,r}]e^{-\frac{t_1}{\tau}}\right)e^{-\frac{(t_2-t_1)}{\tau}}\right)e^{-\frac{(t-t_2)}{\tau}}, & t_2 \leqslant t < T
\end{cases}
\tag{4}
$$

During a switching period, the peak phase currents take place at $t_1$ and $t_2$, then we get the maximum value of current ripple:

$$
\begin{aligned}
\Delta i_{\max} &= i(t_1) - i(t_2) \\
&= \frac{V_{\text{bus}}^*}{\sqrt{3}\,r}\left(2 - 2e^{-\frac{(t_2-t_1)}{\tau}} + e^{-\frac{t_2}{\tau}} - e^{-\frac{t_1}{\tau}}\right) \\
&\quad - i(0_+)\left(e^{-\frac{t_2}{\tau}} - e^{-\frac{t_1}{\tau}}\right).
\end{aligned}
\tag{5}
$$

with $t_1 + t_2 = T$, consequently,

$$
\begin{aligned}
\Delta i_{\max} &= \frac{V_{\text{bus}}^*}{\sqrt{3}\,r}\left(2 - 2e^{-\frac{1-2\frac{t_1}{T}}{\frac{\tau}{T}}} + e^{-\frac{1-\frac{t_1}{T}}{\frac{\tau}{T}}} - e^{-\frac{\frac{t_1}{T}}{\frac{\tau}{T}}}\right) \\
&\quad - i(0_+)\left(e^{-\frac{1-\frac{t_1}{T}}{\frac{\tau}{T}}} - e^{-\frac{\frac{t_1}{T}}{\frac{\tau}{T}}}\right).
\end{aligned}
\tag{6}
$$

Determine $i_{\text{ripple}} = \frac{\Delta i_{\max}}{i(\infty)} \times 100\%$ to express the severity of current fluctuation. Plot current waveforms in math analysis software, Figure 5 shows that the ideal current fluctuation varies with PWM frequency. Here, $i_{\text{ripple\_max}}$ represents $i_{\text{ripple}}$ the maximum value during single PWM period.

It can be clearly seen that:

1. As the PWM carrier frequency increases from 5 kHz to 15,000 by degree, the current fluctuation tends to be smoother.
2. The maximum value of $i_{\text{ripple\_max}}$ is 200%, which is easy to understand, during single PWM period, $i(t)$ reaches $i(\infty)$ and $-i$), while switching period is much longer than $\tau$.
3. $i_{\text{ripple}}$ varies periodically and $i_{\text{ripple\_max}}$ always occurs at a fixed position during $2\pi$ electrical angle.

Base on above conclusion (3), we take the assumption that when $\frac{t_1}{T} = a$ $(0 < a < \frac{1}{2}$, as a certain contant), $i_{\text{ripple}} = i_{\text{ripple\_max}}$. More precisely, $i_{\text{ripple\_max}}$ always occurs at the same duty ratio over an electrical angle cycle of $2\pi$
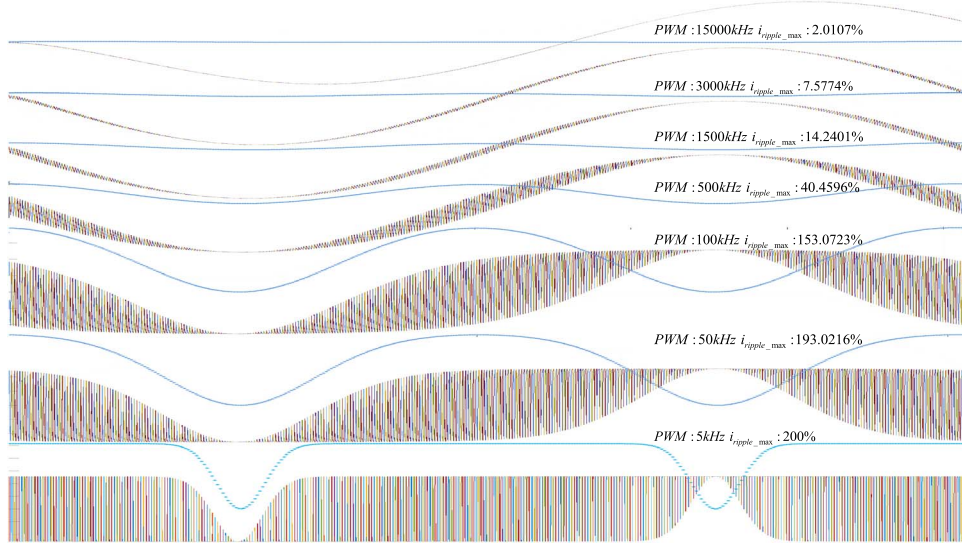
**Figure 5.** Current fluctuation varies with PWM frequency in the electrical angle range of $2\pi$: the colorful line represents phase current waveform and the blue line $i_{\text{ripple}}$ fluctuation.

regardless of PWM frequency. In that,

$$i_{\text{ripple\_max}} = (2 - 2e^{-\frac{1-2a}{T}} + e^{-\frac{1-a}{T}} - e^{-\frac{a}{T}})$$
$$- \frac{i(0_+)}{\frac{V_{\text{bus}}^*}{\sqrt{3}\,r}}(e^{-\frac{1-a}{T}} - e^{-\frac{a}{T}}). \qquad (7)$$

Let $\frac{i(0_+)}{\frac{V_{\text{bus}}^*}{\sqrt{3}\,r}} = \frac{i(0_+)}{i(\infty)} = b$ $(-1 < b < 1)$, and define $e^{-\frac{1}{T}} = x$, Equation (7) can be rewritten as:

$$i_{\text{ripple\_max}} = 2 - 2x^{1-2a} + x^{1-a} - x^a - b(x^{1-a} - x^a). \qquad (8)$$

Apparently, when the PWM frequency increases gradually, the switching period $T$ shall decrease, $\frac{1}{T} \to 0$, then $e^{-\frac{1}{T}} = x \to 1$, likely when the PWM frequency goes down, $\frac{1}{T} \to +\infty$, finally $e^{-\frac{1}{T}} = x \to 0$. Therefore, $x \in (0, 1)$.

It is necessary to analyze the monotonicity of $i_{\text{ripple\_max}}$ to find out detailed mathematical relationship between $i_{\text{ripple\_max}}$ and $x$, which will make above conclusions (1) and (2) more convincing mathematically.

Let

$$f'(x) = \frac{di_{\text{ripple\_max}}}{dx}$$
$$= -2(1-2a)x^{-2a} + (1-b)(1-a)x^{-a} + a(b-1)x^{a-1}$$
$$= \underbrace{x^{-2a}(b-1)}_{<0}$$
$$\times \underbrace{\left[x^a(a-1) + ax^{3a-1} - \frac{2(1-2a)}{b-1}\right]}_{g(x)}.$$

Consider $g'(x) = ax^{a-1}[a-1+(3a-1)x^{2a-1}]$, when $0 < a < \frac{1}{3}$, the part of $g'(x)$, $[a-1+(3a-1)x^{2a-1}]$ is apparently monotonically increasing, i.e., $[a-1+(3a-1)x^{2a-1}] \xrightarrow{x\to 1_-} 2(2a-1) < 0$, hence $g'(x) < 0$ and $g(x)$ monotonically decreases, $g(x)_{\min} \xrightarrow{x\to 1_-} \frac{(2a-1)(b+1)}{b-1} > 0$, $g(x) \geqslant g(x)_{\min} > 0$, $f'(x) < 0$; when $a$ equals $\frac{1}{3}$, $g'(x) < 0$, likewise, $f'(x) < 0$; when $\frac{1}{3} < a < \frac{1}{2}$, $[a-1+(3a-1)x^{2a-1}]$ is monotonically decreasing, whose value ranges from plus to minus, causing $g'(x)$ varying identically, $g(x)$ will increase first and then decrease, $g(x)_{\min} \to \min\{g(x)_{x\to 0_+}, g(x)_{x\to 1_-}\} = \min\left\{(2a-1) - \frac{2(1-2a)}{b-1}, -\frac{2(1-2a)}{b-1}\right\} = \frac{(2a-1)(b+1)}{b-1} > 0$, namely $g(x) \geqslant g(x)_{\min} > 0$, $f'(x) < 0$.

In conclusion, $f'(x) < 0$ is always right, so $i_{\text{ripple\_max}}$ always monotonically decreases along with $x$ increasing, in that, $i_{\text{ripple\_max}} \xrightarrow{x\to 1_-} 0$, $i_{\text{ripple\_max}} \xrightarrow{x\to 0_+} 2$. With PWM frequency increasing, $i_{\text{ripple\_max}}$ is on the decrease. These are consistent with the above conclusions (1) and (2) from Figure 5.

## 4. The Experiments of Upscaling PWM Frequency and Adding Inductance

Relevant hardware platform is designed to validate conclusions obtained in the theoretical derivation of Section 3. Figure 6 reveals the details.

### 4.1. Upscaling PWM Frequency

In Figure 7, it is evident that the phase current ripple diminishes as the PWM carrier frequency increases up to 1 MHz. However,
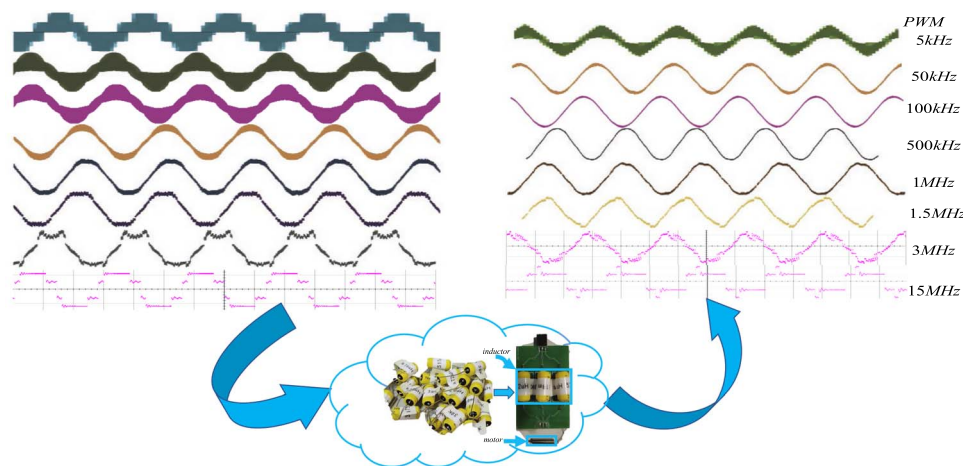
**Figure 6.** Experiment platform.



**Figure 7.** Pratical phase current fluctuation varies with PWM frequency before (left) and after (right) seriesing extra inductor.

as the switching frequency surpasses 1.5 MHz, the degree of the phase current sine worsens, and the phase current nearly becomes six-step commutation with a PWM carrier frequency of 15 MHz. This is quite different from the ideal analysis results obtained in Section 2. The reason why leads to such a difference is that the mosfet is not an absolutely perfect device, but rather has a rising and falling delay when generating signal-level toggle. Besides, MCU's timer has an upper frequency limit. Taking the *STM*32*G*4 as an example, its advanced timer has a maximum frequency of 170 MHz. Hence, when the PWM frequency is 15 MHz, the count of one cycle is only 11, and various SVPWM voltage vectors switch to the same due to the output of rounding in the MCU, resulting in severe current distortion. Both of these key factors combine to determine the resolution of the PWM generator.

### 4.2. Seriesing Inductor

Based on Equation (8), it can be observed that by keeping the PWM frequency constant, if we add a series inductor in the motor circuit, it would increase the value of $\tau$. Consequently,

the value of $x$ would also increase, leading to a decrease in $i_{\mathrm{ripple\_max}}$. To implement this, we purchase lots of inductor 4590R-684K (manufactured by Coilcraft Inc., The USA) with 10% inductance tolerance, and pick out three inductors whose Direct Circuit (DC) resistance and inductance are nearly identical by Inductance Capacitance Resistance (LCR) meter, then series them in motor circuit. This ensured that the time constant $\tau$ increased, and the electrical characteristics of the three-phase circuit of the motor remained consistent.

The inductors we selected out are all near $672\,\mu\mathrm{H}$ and $520\,\mathrm{m}\Omega$, which make $\tau$ increase from 2.49158 to 46.129 $\mu$s. The other experiment conditions are consistent with Section 4.2, and results about the fluctuation of the phase current are obtained in Figure 7:

Apparently, current ripple is significantly suppressed at each PWM frequency spot below 1 MHz, after which the resolution of PWM generator becomes the main limitation. More precisely, it is the upper limit frequency of MCU's timer that leads to such a dilemma.

**Figure 8.** Low-pass model of the motor.

### 4.3. Explanation in Frequency Domain

The fundamental concept of PWM control is transforming direct current into alternating current, whereby the utilization of PWM as a carrier serves to engender an alternating current signal that is commonly referred to as modulation wave. Considering the circuit model of single phase of the three-phase motor is a typical RL series configuration, i.e., a classic low-pass filter as shown in Figure 8. In order for the filter to operate in a desirable fashion, it is critical to ensure that the cut-off frequency is greater than the frequency of the modulating wave while still being less than the frequency of the carrier wave, thereby facilitating the efficient modulation of the alternating current signal.

As for modulation wave,

$$\left| \frac{V_{\text{out}}}{V_{\text{in}}} \right| = \frac{1}{\sqrt{1 + (2\pi f \tau)^2}}. \tag{9}$$

where, $V_{\text{out}}$ represents output of low-pass filter, and $V_{\text{in}}$ input of that. When $2\pi f = \omega_{3\,\text{dB}} = 1/\tau, f = 63.877\,\text{kHz}$, output power of the carrier wave is subject to an abrupt attenuation of 50% of the input power. When the carrier frequency goes on ascending, the carrier wave mixed in the low-frequency current signal exhibits a proclivity to gradually dissipate, thereby resulting in the effective elimination of current ripple. In essence, the salient aim of increasing the carrier frequency or adding inductance primarily rests on the endeavor to further diminish the power of the PWM carrier while concurrently abating the pernicious influence of the PWM carrier on the low-frequency modulation signal (Zhou & Fang 2013).

## 5. High PWM Frequency Control Method based on FOC

It has been observed that the inductor possessing a larger inductance value and a relatively minute direct current resistance tends to have a larger physical size, which renders the incorporation of a seriesing inductor incompatible with certain compact fiber positioners or applications that require size sensitivity. We choose to increase the PWM carrier frequency to control motor. Motor in fiber positioner works in low-speed and making phase current smooth is critical. FOC (Blaschke 1772), a classic sine wave control method, turns into first-preference. Since the absence of an encoder that is commensurate with the $\phi 4\,\text{mm}$ motor, it is necessary to pursue a sensorless drive method, whereby the primary focus on the sensorless closed-loop control, which operates based on the underlying principles of the following two cardinal tenets:

1. Detect the variations of the windings inductance which is caused by the change of the magnetic flux while rotor spins.
2. On the basis of BEMF detection.

Because the stator of the hollow-cup PM has no iron core, engenders a state of affairs wherein the spin of the rotor does not effectuate any alteration to the magnetic resistance of the inductance magnetic loop. Thus the value of phase inductance remains stable. Additionally, six-step commutation based on BEMF is not applicable at low speed because of hollow-cup PM's small BEMF constant $0.059\,\text{mV}\,\text{rpm}^{-1}$, not to mention the fact that square wave commutation elicits a problematic vibration that can engender deleterious effects on the wearing and precision of the mechanic (Jenni et al. 2014). Therefore, this paper proposes an open-loop FOC method to realize the low-speed positioning control with motor that exhibits a small electrical time constant.

Equation (10) puts the $d$–$q$ axis voltage equation (Li & Liu 2009):

$$\begin{cases} V_d = rI_d + L_d \dfrac{dI_d}{dt} - L_q I_q \omega_e \\[2mm] V_q = rI_q + L_q \dfrac{dI_q}{dt} + (L_d I_d + \varphi_f)\omega_e \end{cases} \tag{10}$$

where, $V_d$, $V_q$ represent $d-$ and $q-$ axis stator voltage respectively, $I_d$, $I_q$ are $d-$ and $q-$ axis armature current, and $\omega_e$ is rotor electric angular speed. Control expectation is that $\frac{dI_d}{dt} \to 0, \frac{dI_q}{dt} \to 0$. Then Equation (10) is simplified as:

$$\begin{cases} V_d = rI_d - L_q I_q \omega_e \\ V_q = rI_q + L_d I_d \omega_e + \varphi_f \omega_e \end{cases} \tag{11}$$

Let

$$\begin{cases} V_d^* = V_d + L_q I_q \omega_e = rI_d \\ V_q^* = V_q - \varphi_f \omega_e = rI_q + L_d I_d \omega_e \end{cases}$$

$I_d$ is desired to be zero, hence,

$$\begin{cases} V_d^* = V_d + L_q I_q \omega_e = 0 \\ V_q^* = V_q - \varphi_f \omega_e = rI_q + L_d I_d \omega_e \end{cases}$$

The open-loop control aims to make $V_d^*$ equal zero, and regulates $V_q^*$ to tune $I_q$, in that, proper driving torque will be found out. Figure 9 illustrates the detailed logic of open-loop control.
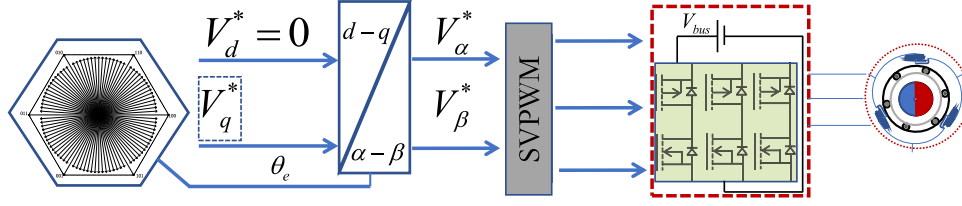
**Figure 9.** Control logic of open-loop FOC.

According to the results of Section 4.2, we decided to adopt 1 MHz PWM switching frequency with $V_{bus}$ equaling 3.3 V. The period for a voltage vector in the open-loop control is 2 $\mu$s, while the calculation time of a voltage vector in MCU consumes 0.9 $\mu$s, which is fair adequate. The $2\pi$ electrical angle is expressed in Q15 ($-32768 \sim 32767$, 1 bit represents the sign position, and 15 bits represent the variable in a 16-bit stored data), and count is incremented by 2 in timer, i.e., the electrical angle increment is $\frac{45}{4096}$°. The voltage vector undergoes a staggering 32,768 commutations over the course of a single rotation of the motor. The increased number of electronic commutations makes the motor phase current change more continuously and smoothly.

Besides, the motor rotates at a constant speed of $\frac{15625}{1024\ \text{rps}}$rps. The commutation time of a single voltage vector amounts to a mere 2 $\mu$s. The number of commutating per revolution serves as a key determinant of both the rotation speed of the motor as well as the overall smoothness of the phase current. It stands to reason that a higher number of commutations per revolution would lead to a slower motor rotation speed while concurrently resulting in a smoother phase current.

In the above case, the peak phase current we test with the hall current probe is 25 mA, so $\sqrt{I_d^2 + I_q^2} = 25$ mA, since $I_d$ almost equals zero, we get $I_q = 25$ mA. $V_d = -L_q I_q \omega_e = 37\ \mu\text{H} \times 25\ \text{mA} \times 2\pi \times -15625/1024 = -88.7\ \mu\text{V}$, the maximum value of $V_d$ in program is 32 767, practically corresponding to $\frac{11\sqrt{3}}{10}V(3.3\ \text{V}/\sqrt{3})$, in programming, $V_{d\_value} = -88.71 \times 10^{-6}/11\sqrt{3}/10 \times 32\ 767 \simeq -2$. On the other hand, $V_q - \varphi_f \omega_e = rI_q$, $\varphi_f \omega_e$ remains constant, so $V_q \propto rI_q$. However, there is a phase difference ignored in Equation (11), here is the supplementary explanation why such neglect does not matter: the model of motor is a RL series circuit, the voltage across the inductor leads the current through it, this phase difference is also reflected in the differential term $L_q \frac{dI_q}{dt}$ of Equation (10). Also

$$\tan \vartheta = \frac{\omega_e L_q}{r}$$

$$= \frac{2\pi \times 15\ 625/1024 \times 37 \times 10^{-6}}{14.85} = 2.388774755 \times 10^{-4}$$
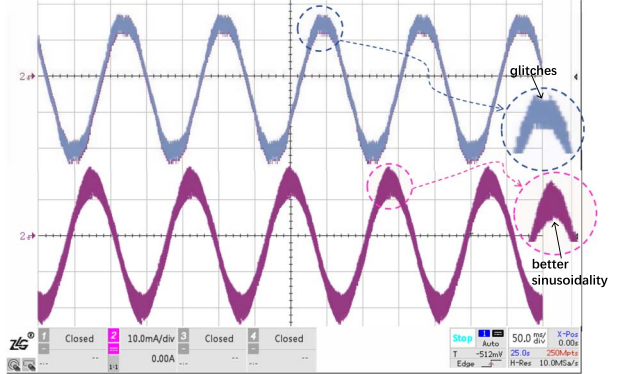


**Figure 10.** Blue waveform is driven by *STSPIN*233, and red waveform MCU directly.

we obtain $\vartheta = 0°0137$, the phase difference hereby can basically be neglected.

Under the equipment conditions shown in Figure 6, regulate directly the setting value of $V_{q\_value}$ to tune the torque of positioning control. When $V_{q\_value} = 10000$, the fiber positioner can run smoothly. Simultaneously, the peak current measured in the oscilloscope is merely 25 mA, which is quite a small current that could be effectively driven directly by the mosfet inside the MCU. As such, we could optimized the hardware configuration further, which might conceivably involve eliminating the extraneous driver Integrated Circuit (IC) *STSPIN*233 in Figure 6.

Figure 10 exhibits the fluctuations of the phase current while utilizing MCU directly drive the motor.

The experimental conditions remained constant throughout, there is no visible difference about the peak value of the phase current, but the sine degree of current has certain improvement. When the MCU is deployed to drive the motor directly, since the rising and falling edges of the mosfet are merely determined by the internal power bridges, the ramping time of chopper is reduced, the current waveform is destined to be improved in accordance with expectation.
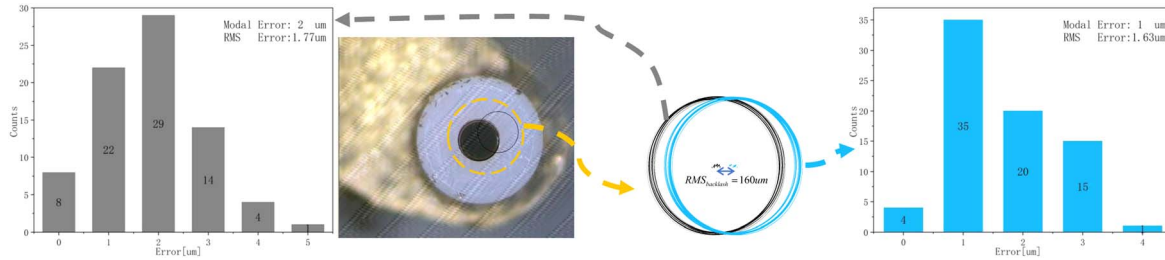
**Figure 11.** Positioning experiment results.

# 6. Positioning Experiment Results and Discussion

## 6.1. Positioning Experiment Results

The digital universal microscope 19JC is a high-precision optical measuring instrument with high-resolution image measuring system. We utilize ceramic head on fiber as microscope's optical measurement target, i.e., the center of the ceramic head, then drive the central rotary axe of SCARA to implement a back and forth movement of a full circle, record ceramic head's central coordinate after every positioning operation. Figure 11 shows the results of the positioning experiment:

We discover that the center coordinates of ceramic head do not coincide at one position, but swing back and forth in two primary positions, which indicates that there is a certain backlash in the mechanical structure of the fiber positioner. After a full circle of central axe's motion, the mechanical clearance brings a 160 $\mu$m error to the fiber ceramic head. The histogram of positioning errors in Figure 11 gives the repeatable positioning error of fiber positioner at two fixed coordinates, both of which are merely several $\mu$m. Compared to mechanical clearance, repeatable positioning error is quite light. Results of positioning experiment validate the engineering feasibility of the open-loop positioning control method based on FOC proposed in this paper. Additionally, the proposed method only takes about 25 mA phase current at most, and the internal mosfets of the MCU can completely afford to, which not only reduces the cost of the hardware case, but also saves valuable physical space for fiber positioner.

## 6.2. Discussion: Switching Losses

When driving a Mosfet with a carrier frequency as high as 1 MHz, an immediate concern might be: will the switching losses of the power device increase dramatically and adversely affect the system? To figure it out, this section provides a detailed assessment of this issue.

Mosfet (Metal-Oxide-Semiconductor Field-Effect Transistor), is the most important component in low-voltage and low-power motor drive systems. During the Mosfet turn-on process, as the $V_{DS}$ voltage decreases, the $I_D$ current gradually increases, and there will be an overlap between voltage and current,
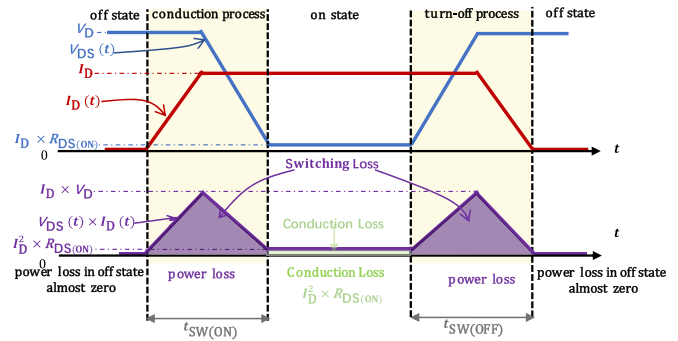


**Figure 12.** switch transition process of Mosfet.

resulting in power losses. When the Mosfet is fully conducting, the $V_{DS}$ voltage is not equal to zero due to the conducting resistance between the DS terminals, resulting in voltage drop and power loss. The turn-off process of Mosfet is similar to the turn-on process, so the turn-off process also generates losses. When making recommendation of MHz PWM frequency for the motor, we must consider the impact of switching losses.

Generally speaking, the principle of switch loss in the operation of a Mosfet is shown in Figure 12. The relationship graph between the drain-source voltage $V_{DS}(t)$ and drain-source current $I_D(t)$ can well explain the switch loss during the transition process. As shown in the upper waveform, there is a transient voltage and current during the $t_{SW(ON)}$ and $t_{SW(OFF)}$ periods, and the Mosfet capacitance is charged and discharged. Before the $V_{DS}(t)$ drops to the final conduction state ($V_{DS}(t) = I_D \times R_{DS(ON)}$), the full load current $I_D$ flows through the Mosfet. Conversely, during turn-off, $V_{DS}(t)$ gradually rises to the final value of the turn-off state before the Mosfet current drops to zero. The overlapping part of voltage and current during the switching process is the source of switching loss. The main power loss during the entire process is reflected in the "conduction process," "turn-off process," and "conduction state," while the loss in the turn-off state is very small and can be neglected.

Switching losses are caused by the non-ideal behavior of the switch, and it is difficult to accurately calculate the switching losses of Mosfets and diodes. Typically, the switching losses

can be estimated based on the triangular waveform in Figure 12, using the following formula:

$$P_{\text{SW}} = \frac{1}{2} V_D I_D (t_{D(\text{ON})} + t_{\text{SW(OFF)}}) f_s. \tag{12}$$

Here $V_D$ is the drain-source voltage when the Mosfet is turned off, $I_D$ is the channel current when the Mosfet is turned on, $t_{\text{SW(ON)}}$ and $t_{\text{SW(OFF)}}$ are the turn-on and turn-off times, respectively. These parameters can be obtained from the Mosfet datasheet. $t_{\text{SW(ON)}}$ is the sum of turn-on delay time $t_{D(\text{ON})}$ and rise time $t_{\text{rise}}$, while $t_{\text{SW(OFF)}}$ is the sum of turn-off delay time $t_{D(\text{OFF})}$ and fall time $t_{\text{fall}}$.

The datasheet of *STSPIN*233 only provides typical values of $t_{\text{rise}}$ and $t_{\text{fall}}$. For the unknown parameters of $t_{D(\text{ON})}$ and $t_{D(\text{OFF})}$, $t_{\text{rise}}$ and $t_{\text{fall}}$ are used as a substitute, because the turn-on/turn-off delay times are usually not much different from the rise/fall times. $I_D$ is assumed to be the peak phase current of 25 mA, $V_D$ is assumed to be the bus voltage of 3.3 V, and the carrier frequency is 1 MHz. The switching power loss is calculated as $P_{\text{SW}} = \frac{1}{2} \times 3.3 \text{ V} \times 25 \text{ mA} \times (10 + 10) \times 10^{-9}\text{s} \times 1 \times 10^6\text{Hz} = 0.825$ mW. The conduction loss is $P_{COND} = I_D^2 R_{\text{DS(ON)}} = (25 \text{ mA})^2 \times 0.4 \text{ }\Omega = 0.25$ mW. Even at a carrier frequency of 1 MHz, the switching power loss of the Mosfet is only comparable to the conduction loss, and the average conduction time in a 1 $\mu$s period is much greater than 20 ns, so the conduction loss still dominates and switching loss is not significant enough to cause too much attention.

## 7. Conclusion

Because of compact structure, miniature hollow-cup PM is widespreadly utilized in notebook fans, electric toothbrushes or certain space-constrained applications, which facilitates typical drive control of rotation without concern for detailed speed-tuning. As the actuator of moving optical fiber in astronomical telescopes system, fiber positioner is usually required to be manufactured as small as possible to obtain more excellent spectral coverage (Martini et al. 2018). To meet the size-sensitive demands of such applications, miniature hollow-cup PM also plays an indispensable part in precision positioning control, especially for fiber positioner (Leitner et al. 2018) with compact mechanical structures. However, encoders are not originally included in the design of the compact positioner due to a lack of cost effective commercially available encoders at the very small sizes needed (Fisher et al. 2009). Smaller fiber positioners invariably encounter this problem during design process. If a viable (small and cheap) encoder can be found it would likely resolve the dilemma of low efficiency in open-loop control. Therefore, we have to adopt an open-loop control strategy similar to DESI (Collaboration, D. et al. 2022) to fulfill the precise positioning requirement in MOS. Obviously, this is a way of sacrificing efficiency to achieve the goal.

Compared to the use of a stepper method to control 25 mA in fiber positioner (where phase current reaches as high as 66 mA Guo et al. 2022), deploying open-loop FOC control based on voltage only takes 25 mA phase current and 3.3 V bus voltage. Under the high carrier frequency control mode, with each full rotation of the motor, up to 32768 electronic commutations ensure a smooth and continuous motor current with a smaller peak value. The current consumption is much smaller than the open-loop drive used in DESI, which can consume hundreds of mA (Martini et al. 2018). Such a small phase current is sufficient to drive the motor using the MCU's built-in Mosfet bridge without additional voltage rails, saving on power devices and buck components, reducing costs, and also saving valuable PCB (the Printed Circuit Board) space. The voltage-open-loop FOC drive for fiber positioner can also keep up with the time consumption of the stepper method, meaning that the open-loop FOC is more efficient without the problem of passive holding torque that the stepper controller has. Taken together, the results of this paper can inform the present and future miniature hollow-cup PM control of fiber positioner or positioning control of precision instruments with compact design.

## References

Araujo, R., Bouri, M., Brandon, C., et al. 2020, Design of a Theta/Phi fiber positioner robot for the Sloan Digital Sky Survey V, Proc. SPIE, 11447, 1144790

Aydin, M., & Gulec, M. 2016, A New Coreless Axial Flux Interior Permanent Magnet Synchronous Motor With Sinusoidal Rotor Segments, ITM, 52, 1

Besuner, R., Bebek, C., Dey, A., et al. 2012, Integrating BigBOSS with the Mayall Telescope, Proc. SPIE, Vol. 8446, 844652

Blaschke, F. 1772, The principle of field orientation as applied to the new TRANSVECTOR closed loop control system for rotating field machines, Siemens Rev, 34, 217

Casadei, D., Profumo, F., Serra, G., & Tani, A. 2002, FOC and DTC: two viable schemes for induction motors torque control, ITPE, 17, 779

Cirasuolo, M., Afonso, J., Carollo, M., et al. 2014, MOONS: the Multi-Object Optical and Near-infrared Spectrograph for the VLT, Proc. SPIE, 9147, 91470N

Collaboration, D., Abareshi, B., Aguilar, J., et al. 2022, Overview of the Instrumentation for the Dark Energy Spectroscopic Instrument, AJ, 164, 207

Cui, X., Su, D., Li, G., et al. 2004, Experiment system of LAMOST active optics, Proc. SPIE, 5489, 974

Cui, X. Q., Zhao, Y. H., Chu, Y. Q., et al. 2012, The Large Sky Area Multi-Object Fiber Spectroscopic Telescope LAMOST, RAA, 12, 1197

Diehl, H. T., Abbott, T. M. C., Bailey, J., et al. 2010, Testing the Dark Energy Camera on a telescope simulator, Proc. SPIE, 7735, 77353I

Fahim, N., Prada, F., Kneib, J. P., et al. 2015, An 8-mm diameter fibre robot positioner for massive spectroscopy surveys, MNRAS, 450, 794

Fang, J., Li, W., & Li, H. 2014, Self-Compensation of the Commutation Angle Based on DC-Link Current for High-Speed Brushless DC Motors With Low Inductance, ITPE, 29, 428

Fang, J., Zhou, X., & Liu, G. 2013, ITPE, 28, 1400

Fisher, C., Braun, D., Kaluzny, J., & Haran, T. 2009, Cobra: A two-degree of freedom fiber optic positioning mechanism, in 2009 IEEE Aerospace conference *(Big Sky, Montana, USA)* (IEEE), 1

Flaugher, B. 2006, The Dark Energy Survey instrument design, Proc. SPIE, 6269, 62692C

Guo, S. X., Zhai, C., & Bi, S. L. 2022, Low voltage optical fiber positioner robot based on minimum inductance hollow cup motors, Low voltage optical fiber positioner robot based on minimum inductance hollow cup motors 1, University of Science and Technology of China, 12

Hörler, P., Kronig, L., Kneib, J.-P., et al. 2018, High density fiber positioner system for massive spectroscopic surveys, MNRAS, 481, 3070

Hu, H., Peng, X., Zhai, C., Li, W., & Xing, X. 2004, Study on the optical fiber positioning medium-term system for LAMOST, Proc. SPIE, 5492, 574

Hu, H., Wang, J., Liu, Z., et al. 2014, A high-density integrated optical focal plane positioning system, Proc. SPIE, 9151, 91514R

Jenni, L., Hörler, P., Makarem, L., et al. 2014, Developing micro DC-brushless motor driver and position control for fiber positioners, Proc. SPIE, 9147, 914744

Kronig, L., Hörler, P., Caseiro, S., et al. 2020, Optical test procedure for characterization and calibration of robotic fiber positioners for multiobject spectrographs, JATIS, 6, 018001

Kronig, L., Hörler, P., Kneib, J.-P., & Bouri, M. 2018, Design and performances of an optical metrology system to test position and tilt accuracy of fiber positioners, Proc. SPIE, 10706, 107066B

Lai, Y.-S., Lee, K.-Y., Tseng, J.-H., Chen, Y.-C., & Hsiao, T.-L. 2007, Efficiency Comparison of PWM-Controlled and PAM-Controlled Sensorless BLDCM Drives for Refrigerator Applications, in 2007 IEEE Industry Applications Annual Meeting *(New Orleans, LA, USA)* (IEEE), 268

Leitner, D., Aguilar, J., Ameel, J., et al. 2018, Proc. SPIE, 10706, 1070669

Li, S., & Liu, Z. 2009, Adaptive Speed Control for Permanent-Magnet Synchronous Motor System With Variations of Load Inertia, ITIE, 56, 3050

Liu, G., Fang, J., & Liu, J. 2008, Research Progress on the Application of High-speed Brushless DC Motor in Magnetically Suspended Inertial Actuator, Meas. Control, 41, 88

Martini, P., Bailey, S., Besuner, R. W., et al. 2018, Overview of the Dark Energy Spectroscopic Instrument, Proc. SPIE, 10702, 107021F

Montgomery, D., Atkinson, D., Beard, S., et al. 2016, Development of the fibre positioning unit of MOONS, Proc. SPIE, 9908, 990895

Oliveira, A. C., Jacobina, C. B., & Lima, A. M. N. 2007, Improved Dead-Time Compensation for Sinusoidal PWM Inverters Operating at High Switching Frequencies, ITIE, 54, 2295

Park, S. J., Park, H. W., Lee, M. H., & Harashima, F. 2000, A new approach for minimum-torque-ripple maximum-efficiency control of BLDC motor, ITIE, 47, 109

Pérez-Calpena, A., Mancera, E. S.-B., Gomez-Alvarez, P., et al. 2018, MEGARA MOS: Where are my positioners and fibers pointing to?, Proc. SPIE, 10706, 107062C

Sayres, C., Sánchez-Gallego, J. R., Blanton, M. R., et al. 2021, SDSS-V Algorithms: Fast, Collision-free Trajectory Planning for Heavily Overlapping Robotic Fiber Positioners, AJ, 161, 92

Sosa, M. S., von Essen, C., Andruchow, I., & Cellone, S. A. 2017, Impact of seeing and host galaxy into the analysis of photo-polarimetric microvariability in blazars - Case study of the nearby blazars 1ES9+650 and HB891+044, A&A, 607, A49

Sun, J., Xing, G., Zhou, X., & Sun, H. 2022, Static magnetic field analysis of hollow-cup motor model and bow-shaped permanent magnet design, ChJA, 35, 306

Tsotoulidis, S., & Safacas, A. N. 2015, Deployment of an Adaptable Sensorless Commutation Technique on BLDC Motor Drives Exploiting Zero Sequence Voltage, ITIE, 62, 877

Xiaofeng, Z., & Zhengyu, L. 2006, in 2006 CES/IEEE 5th International Power Electronics and Motion Control Conference, 3 *(Shanghai, China)* (IEEE), 1

Zeroug, H., Boukais, B., & Sahraoui, H. 2002, Analysis of torque ripple in a BDCM, ITM, 38, 1293

Zhou, X., Chen, X., Zeng, F., & Tang, J. 2017, Fast Commutation Instant Shift Correction Method for Sensorless Coreless BLDC Motor Based on Terminal Voltage Information, ITPE, 32, 9460

Zhou, X., & Fang, J. 2013, Precise Braking Torque Control for Attitude Control Flywheel With Small Inductance Brushless DC Motor, ITPE, 28, 5380